doi:10.2533/chimia.2022.661 Chimia 76 (2022) 661–668 © A. deMello *et. al.*

Hybrid Microfluidic Device for High Throughput Isolation of Cells Using Aptamer Functionalized Diatom Frustules

Rashin Mohammadi[ab], Mohammad Asghari[a], Monika Colombo[a], Zahra Vaezi[c], Daniel A. Richards[a], Stavros Stavrakis[a], Hossein Naderi-Manesh*[b], and Andrew deMello§*[a]

§Simon-Widmer Award 2021

Abstract: Circulating tumor cells (CTCs), secreted from primary and metastatic malignancies, hold a wealth of essential diagnostic and prognostic data for multiple cancers. Significantly, the information contained within these cells may hold the key to understanding cancer metastasis, both individually and fundamentally. Accordingly, developing ways to identify, isolate and interrogate CTCs plays an essential role in modern cancer research. Unfortunately, CTCs are typically present in the blood in vanishingly low titers and mixed with other blood components, making their isolation and analysis extremely challenging. Herein, we report the design, fabrication and optimization of a microfluidic device capable of automatically isolating CTCs from whole blood. This is achieved in two steps, *via* the passive viscoelastic separation of CTCs and white blood cells (WBCs) from red blood cells (RBCs), and subsequent active magnetophoretic separation of CTCs from WBCs. We detail the specific geometries required to balance the elastic and inertial forces required for successful passive separation of RBCs, and the use of computational fluid dynamics (CFD) to optimize active magnetophoretic separation. We subsequently describe the use of magnetic biosilica frustules, extracted from *Chaetoceros sp.* diatoms, to fluorescently tag CTCs and facilitate magnetic isolation. Finally, we use our microfluidic platform to separate HepG2-derived CTCs from whole blood, demonstrating exceptional CTC recovery (94.6%) and purity (89.7%)

Keywords: Circulating tumor cells · Diagnostics · Microfluidic platform

Andrew deMello received his bachelor degree in Chemistry from Imperial College London. After completing his PhD in Molecular Photophysics at the same university, he took up a postdoctoral fellowship at the University of California, Berkeley working with Professor Richard Mathies on early microfluidic systems for DNA analysis. After returning to the UK, Andrew became Professor of Chemical Nanosciences at Imperial College London. He moved to ETH Zurich in 2011, where he now holds the Chair of Biochemical Engineering. His group's research interests lie in the general area of microfluidics and nanoscale science. Primary specializations include the development of microfluidic devices for high-throughput biological and chemical experimentation, ultra-sensitive optical detection techniques and the exploitation of point-of-care diagnostic technologies. Andrew has given approximately 450 invited lectures (including 100 plenary or keynote lectures) describing these activities and has published 400 papers in the peer-reviewed literature.

Introduction

Despite concerted efforts from scientists and medical professionals, cancer remains a leading cause of death globally. Methods for detecting cancer can decrease morbidity and mortality by facilitating timely medical intervention and limiting metastasis.[1] Unfortunately, the complex nature of oncological diseases creates significant diagnostic challenges. Cancer biomarkers are often present in low titers, are frequently non-specific and can vary significantly in both identity and concentration from patient to patient.[2] This is particularly true for non-invasive liquid biopsies, *e.g.* blood test biomarkers. Accordingly, the gold-standard for many cancer diagnoses remains the (invasive) needle biopsy. Recently, the isolation of intact and viable circulating tumor cells (CTCs) has been championed as a non-invasive tool in cancer diagnosis and prognosis, as well as in drug screening and treatment efficacy monitoring.[3] However, CTC isolation is challenging, primarily due to their low blood titers relative to other cells, *e.g.* leukocytes and erythrocytes.[4] In recent years, microfluidic systems have emerged as promising tools for fast, efficient, robust isolation of micron-sized species, including CTCs, from biofluids.[5] Such systems can be classified as passive or active in nature, depending on the manipulating forces involved. Passive methods such as pinched flow fractionation (PFF), inertial microfluidics and deterministic lateral displacement (DLD) solely rely on effecting separation using geometrical, physical, and fluid properties.[6] However, while PFF and inertial approaches are cost-effective and easy to use in a high throughput manner, they rely almost exclusively on variations in species size to achieve separation and thus are incapable of resolving similarly sized particles. DLD has been previously utilized for the isolation of CTCs; however, its widespread application in CTC diagnostics is compromised by its

*Correspondence: Prof. H. Naderi-Manesh[b], E-Mail: naderman@modares.ac.ir; Prof. A. deMello[a], E-mail: andrew.demello@chem.ethz.ch
[a]Department of Chemistry and Applied Biosciences, ETH Zurich, Vladimir Prelog Weg 1, CH-8093 Zurich, Switzerland; [b]Department of Nanobiotechnology/Biophysics, Faculty of Biological Sciences, Tarbiat Modarres University, Tehran, 14115-154, Iran; [c]Department of Bioactive Compounds, Faculty of Interdisciplinary Science and Technologies, Tarbiat Modares University, Tehran, 14115-154, Iran

low throughput nature and propensity to block.[6–8] Alternatively, active methods such as magnetophoresis,[7,9,10] dielectrophoresis,[11,12] and acoustophoresis[13–15] can be employed to isolate CTCs. These methods involve the application of external forces to cells to achieve sorting, and can be used to resolve similarly sized species, providing that the cells of interest display an intrinsic (or extrinsic) property than can be manipulated (*e.g.* magnetism). Although such approaches can be highly specific, isolating CTCs from whole blood solely using an active approach is highly challenging due to the presence of red blood cells (RBCs). Indeed, RBCs (rich in deoxyhemoglobin or methemoglobin) are intrinsically paramagnetic and present at a high relative concentrations in blood.[16] They can therefore 'shield' target cells from an applied external force, ultimately decreasing separation efficiencies and recoveries. Hybrid microfluidic approaches employing both passive and active separation modalities have the potential to overcome these limitations.[17–21] Such approaches typically involve the passive removal of small RBCs and a certain percentage of white blood cells (WBCs) from a population of target CTCs, and the subsequent active separation of CTCs from the remaining WBCs. Among passive approaches for cell separation, the use of viscoelastic microfluidics has attracted the most attention, due to its ability to separate species over wide size ranges and process biofluids at high volumetric flow rates.[22]

In non-Newtonian viscoelastic fluids, the viscosity of the fluid is not constant but changes as a function of the shear rate. Such variations can be used to introduce additional 'lift' forces that enable the passive focusing and subsequent separation of micron-sized species. Viscoelastic lift forces can be understood in terms of inertial lift (F_i), due to fluid inertia, and elastic lift (F_e), due to fluid elasticity.[23] In simple terms, size-based separations using viscoelastic fluids are achieved by balancing particle size-dependent hydrodynamic forces, where $F_e \propto a^3$ and $F_i \propto a^4$.[24] Such balancing is normally achieved using either: (1) a sheathless single inlet with a non-Newtonian fluid flow, (2) a non-Newtonian sheath fluid with a Newtonian fluid main flow or (3) non-Newtonian sheath and sample fluids.[25] The use of a sheath flow is effective in increasing separation efficiencies by aligning species prior to their lateral migration due to elastic lift forces.[26] In addition, sheath flows are effective in reducing cell–cell interactions by diluting the biological fluid input and minimizing preprocessing steps such as RBC lysis, which may cause CTC loss or damage. Recently, viscoelastic separation using a sheath fluid was shown to allow for the separation of CTCs from whole blood.[26,27] Although recoveries in excess of 77.5% were achieved, purity values were unacceptably low. This suggests the need to integrate an active method to enhance purity.

Amongst active cell sorting techniques, magnetophoresis has attracted interest due to its high specificity, engendered by conjugation of magnetic particles to cells. Magnetophoretic sorting of cells has been shown to be an effective and biocompatible method for sorting cells, and easy to integrate within microfluidic platforms.[28,29] Here cells are tagged with target-specific ligands, such as antibodies, aptamers or peptides, which have previously been conjugated to magnetic particles.[20] Since magnetophoretic manipulations are contactless in nature, they are ideally suited for processing biological samples,[30,31] with a range of functionalized magnetic nanoparticles (*e.g.* iron oxide nanoparticles) being readily available.[32] For example, Huang *et al.* developed a microfluidic device, comprising passive inertial microfluidics and active magnetophoresis, for CTC separation from WBCs.[33] This yielded a recovery rate of 83% but a rather low purity of 19% at an initial $1/10^5$ ratio of CTCs to blood cells. Additionally, Nasiri *et al.* recently reported a similar passive-active method for isolating CTCs from whole blood.[34] Although the method delivered a recovery rate of 89% and purity of 93%, this was achieved using high blood dilutions (20x) and a low CTC to blood cell ratio (1/1000). In addition, the use of EpCAM (anti-epithelial cell adhesion molecule) antibodies is non-optimal since it is not specific to CTCs.

As previously noted, magnetophoretic methods use cells tagged with target-specific ligands, such as antibodies, aptamers and peptides, which have previously been conjugated to magnetic particles.[20] Unsurprisingly, the potential cytotoxicity of common magnetic tags is a significant concern.[35] To counter cytotoxic effects, researchers have begun to explore natural biomaterials as magnetic tags for cell sorting applications, due to their innate biocompatibility. In this regard, diatomic biosilica frustules, isolated from the porous external wall of algae diatoms (such as *Chaetoceros sp.* Plankton) are of interest.[36,37] These micron-scale structures are primarily composed of silica, and arranged into complex 3D microstructures, with a distinctive hierarchical structure. They are biocompatible,[38] have large effective surface areas for functionalization[39] and are cheap and simple to produce. In addition, since diatomic biosilica frustules can be easily cultivated or found in nature, they represent an interesting and accessible alternative to synthetic silica nanoparticles. Diatomic biosilica frustules are also inherently fluorescent, photostable and they contain a high density of nanoscale pores, which can be readily doped with magnetic nanoparticles.[36,40,41] This means that they can be magnetized whilst retaining their biocompatibility.[36] To the best of our knowledge, no previous studies have addressed the use of diatom biosilica frustules as magnetic and multicolor fluorescence probes for CTC separation and detection. Accordingly, we present a hybrid microfluidic device able to separate and measure CTCs from human whole blood in real-time at $1/10^7$ ratio of CTCs to blood cells. Specifically, we use a two-step passive-active approach, in which passive viscoelastic separation is first used to separate RBCs from CTCs and WBCs, followed by active magnetic separation of CTCs from WBCs. Aptamer-targeted, iron-oxide doped biosilica frustules are used as magnetic and fluorescent tags for both isolating and detecting CTCs. The effectiveness of the platform is demonstrated by the successful separation of HEPG2-presenting CTCs from whole blood samples, and validation of the process using flow cytometry.

Experimental Section

Device Design and Fabrication

Conventional photolithography was used to fabricate a microfluidic master mold. Briefly, microchannel patterns were designed using AutoCAD 2019 (Autodesk, San Rafael, USA) and printed onto 177 μm-thick fine grain emulsion film (Micro Lithography Services, Chelmsford, UK) to form a photomask. This photomask was then used to pattern an SU-8 coated silicon wafer (Microchem, Massachusetts, USA). Details of this process are provided in the Electronic Supplementary Information. The final microfluidic device comprises two separate regions for viscoelastic and magnetic separation. The viscoelastic unit consists of two center inlets; one for whole blood and the other for the viscoelastic sheath fluid, while outlet 1 is used to collect RBCs. Viscoelastic separation was performed within a straight square microchannel (width 50 μm, height 50 μm) with a total length of 4 cm ending in three outlets. The side outlets are used to extract RBCs and small WBCs. The central outlet was designed to collect CTCs and larger WBCs and is followed by the magnetic separation zone. The magnetic separation zone consists of a focusing zone (14 mm long and 50 μm wide) and a separation zone (20 mm long and 800 μm wide). The magnetic field is created by positioning a N45 Neodynium rod magnet and a cubic Neodynium magnet (Supermagnete, Uster, Switzerland) in close proximity (200 μm) to the magnetic sorting channel. A 10:1 mixture of polydimethylsiloxane (PDMS) monomer and curing agent (Sylgard 184, Dow

Corning, Midland, Miami, USA) was poured over the master mold and peeled off after polymerization at 70 °C for 4 hours. Inlet and outlet ports were created using a hole-puncher (SYNEO, Florida, USA). After treating both glass and PDMS surfaces in an oxygen plasma (EMITECH K1000X, Quorum Technologies, East Sussex, United Kingdom) for 60 seconds, the structured PDMS substrate was bonded to a 1 mm thick glass substrate (Menzel-Glaser, Manheim am Rhein, Germany).

Control and Detection System

A syringe pump (CETONI GmbH, Korbussen, Germany) was used to inject sample and core fluids at variable flow rates. To visualize particles and cells in brightfield mode, the microfluidic device was mounted on an inverted Ti-E microscope (Nikon, Zurich, Switzerland) equipped with a EoSens 3CL high-speed camera (Mikrotron, Unterschleißheim, Germany), and a solid-state, plasma light source (HPLS200, Thorlabs, Bergkirchen, Germany) in conjunction with 20× and 10×, 0.45 NA S Plan Fluor objectives (Nikon, Egg, Switzerland). For fluorescence imaging experiments, 40 µl of a cell suspension in phosphate buffered saline (PBS) was sandwiched between a glass slide and a coverslip, illuminated with an LED lamp (Spectra X, Lumencor, Oregon, USA) and imaged with an ORCA-Flash 4.0 CMOS camera (Hamamatsu, Solothurn, Switzerland).

Sample Preparation

The synthesis of magnetic nanoparticles (Fig. S1), their conjugation to diatom frustules (magnetic diatom frustules:mag@DF) and their morphological analysis (Fig. S2) were performed using previously published protocols,[42] as described in the Electronic Supplementary Information. Viscoelastic fluids were prepared by completely dissolving polyethylene oxide (PEO, MW = 600 kDa, Sigma-Aldrich, Buchs, Switzerland) in PBS to a concentration of 1% (w/v). The produced solution was then aged for one week at 4 °C to ensure steady-state behaviour.[43] Then, 0.1%, 0.15%, 0.2%, 0.25%, and 0.3% (v/v) PEO solutions were prepared by dissolving 1% of the stock PEO in PBS. These solutions were used to assess which PEO concentration in the sheath flow yields optimal separation (Fig. S3). Polystyrene beads (Sigma-Aldrich, Buchs, Switzerland) with average diameters of 12 and 7 µm were added to a 0.1% PEO solution in a 10:1 ratio to act as the sample fluid. For whole blood cell analysis, 500 HepG2 cells conjugated TLS11a-mag@DF were spiked into 10 ml of healthy donor diluted blood (1.5 x 10^8 cells/ml), with a final concentration of 0.1% PEO. All samples were loaded into glass syringes (Hamilton, Reno, USA) and delivered directly into the microfluidic device.

Flow Cytometry

After each experiment, cells were washed and resuspended in PBS. Collected cells were then strained through a 40 µm cell strainer (Fisher Scientific AG, Reinach, Switzerland). Flow cytometry analysis was performed using a CytoFLEX S flow cytometer (Beckman Coulter Life Sciences, Krefeld, Germany). Data were analyzed using FlowJo X v 10.0.7 (Tree Star, Texas, USA) software. First, live cells were gated according to the FSC (forward scattering) vs SSC (side scattering) plot. Subsequently, a plot of SSC at 488nm vs SSC at 405 nm was used to gate RBCs and nucleated cells (CTCs & WBCs) from platelets. Finally, discrimination of CTCs from WBCs was achieved using a 2-color scatter plot of APC (Allophycocyanin) vs FITC signals. Purity and recovery values were calculated using Eqns (1) and (2), respectively,

$$\text{Purity} = (\text{CTCs collected})/(\text{total cells collected})*100 \quad (1)$$

$$\text{Recovery} = (\text{CTCs collected})/(\text{CTCs introduced})*100 \quad (2)$$

Results and Discussion

To properly analyze CTCs in whole blood, it is necessary to separate them from both RBCs and WBCs. This is achieved using both passive and active mechanisms. In our device, separation of CTCs is achieved *via* passive viscoelastic separation of WBCs & CTCs from RBCs, flow-focusing of the CTCs and WBCs and finally active magnetic separation of the CTCs from WBCs. In each stage, the desired function was achieved by exploiting a unique microfluidic geometry (Fig. 1).

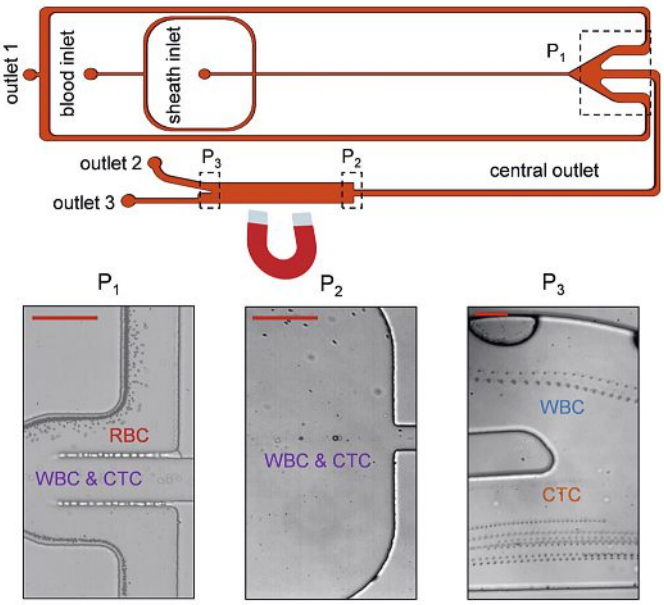

Fig. 1. Schematic and stacked images of the hybrid passive–active microfluidic device for magnetophoretic separation of CTCs from whole blood. The hybrid microfluidic device comprises three parts: (P1) A viscoelastic size-based separation to discriminate CTCs and WBCs from RBCs; (P2) A cell focusing structure to focus the WBCs and CTCs into a single file and (P3) A magnetic separation unit which allows isolation of the magnetically tagged CTCs from native WBCs. Scale bars:100 µm.

Viscoelastic Separation of RBCs from CTCs and WBCs

To facilitate passive viscoelastic sorting, we designed a portion of the microfluidic device to contain a square cross-section microchannel (55 µm high, 55 µm wide and 4500 µm long) with two inlets for the blood sample and sheath fluid and three outlets for RBC (outlet1), WBC (outlet 2) and CTC (outlet 3) isolation. The outlets consist of one central channel and two side channels. The optimal flow rates of both the sample and sheath flows for the separation of CTCs and WBCs from RBCs were determined by flowing two populations of polystyrene beads (having average diameters of 7 and 12 µm) in PBS buffer containing PEO, through the channel and analyzing the images from the side and central outlets (Fig. 2). The polystyrene bead sizes were chosen due to their similarity to the sizes of RBCs and WBCs/CTCs, respectively.[44] The data suggest that optimal separation efficiency is achieved using a sample flow rate (0.1% PEO) of 300 µl/h and a sheath flow rate (0.3% PEO_{600}) of 1300 µl/h (Fig. 2B). Under these conditions, the majority of smaller particles remain in the sample fluid near the channel sidewalls, and are eliminated *via* the side outlets. Conversely, larger particles move towards the center of the flow and pass through the central outlet. These results can be rationalized by considering the competition between the elastic ($F_e \sim a^3$) and inertial ($F_i \sim a^4$) forces acting upon particles.[45,46] For the optimum sheath flow rate, the dominant elastic force moves the larger (12 µm) particles through the fluid interface and towards the channel centerline. Smaller (7 µm) particles remain in

the sample fluid and in the vicinity of the channel edge, since the elastic forces are not strong enough to move them through the fluid interface and into the core flow.[45,46]

Next, the separation performance of the device was investigated using spiked whole blood samples. In this case we experimentally determined the optimal PEO concentration of the sheath flows at 0.3%. The separation efficiency was then examined as a function of sheath flow rate, whilst keeping the sample flow rate constant at 300 µl/h. The ratios of WBCs+CTCs, and RBCs collected from the central outlet was then determined by flow cytometry (Fig. 3). At a sheath flow rate of 800 µl/h the central outlet stream consisted of 16.4% RBCs. This was reduced to 10.7% at a sheath flow rate of 1300 µl/h. Increasing the sheath flow rate further to 1500 µl/h reduced the separation efficiency, with the central outlet stream comprising 52.6% RBCs. Data are consistent with the bead separation data, where the highest separation efficiency occurred for a core flow rate of 1300 µl/h and a sample flow rate of 300 µl/h. Visual inspection of the eluent from the outlets and the raw sample at the inlet can also be used to judge the efficiency of RBC separation (Fig. S4). Spiked blood at the inlet is red in color due to the presence of RBCs. However, after transiting the first stage, RBCs are separated from nucleated cells, with the eluent from the central channel outlet being light beige in color, confirming the exclusion of RBCs. Conversely, the eluent from the side channel retains a red hue, confirming the presence of RBCs. As with bead-based experiments, data show that careful balancing of F_e and F_i is necessary to direct larger WBCs (primarily 15–30 µm diameter monocytes and 12–15 µm diameter granulocytes) and CTCs into the central flow. If the sheath flow rate is too low (*e.g.* 800 µl/h, Re = 1.025 and Wi = 1.34), the elastic force is insufficient to focus the CTCs and WBCs into the centerline. Conversely, if the sheath flow rate is too high (1500 µl/h, Re = 1.66 and Wi = 2.24), the dominant elastic force causes centerline migration even for the smaller RBCs, thus compromising purity. At the optimized flow rate (1300 µl/h, Re = 1.49 and Wi = 1.9), elastic forces are high enough to force WBCs and CTCs into the central flow stream, whilst the RBCs and smaller WBCs remain close to the walls and exit *via* the side outlets (Movie S1).

Magnetic Separation of CTCs from WBCs

To separate CTCs from WBCs, we employed a magnetophoretic purification strategy.[28,29] To do this, it was first necessary to magnetize target CTCs. We achieved this through the use of CTC-targeted magnetic biosilica diatom frustules. For the purposes of this study,[42] tagging of magnetized frustules with CTCs was achieved *via* surface functionalization with the aptamer, TLS11a. This aptamer is known to target hepatoma cells such as CTCs derived from HepG2.[47–49] We first aminated the magnetic frustules using (3-aminopropyl)triethoxysilane (APTES), and then crosslinked them to TLS11a, which contains a terminal amine, using glutaraldehyde. At each stage of the reaction, we characterized the frustules using FTIR, UV-Vis and fluorescence spectroscopy (Fig. 4). The emergence of the distinct NH_2 bending and stretching vibrational modes at 1400 and 2973 cm^{-1}, respectively, and a decrease in the Si-O-Si bending mode of the diatom biosilica at 1033 cm^{-1} confirm successful amination upon reaction with APTES (Fig. 4A, blue). The disappearance of the NH_2 peaks after incubation with glutaraldehyde and TLS11a indicates that the desired condensation reaction has occurred (Fig. 4A, red). In addition, a peak at 1600 cm^{-1} that corresponds to NH bending, confirms glutaraldehyde and TLS11a aptamer reaction. An increase in the absorbance at 280 nm of the aminated magnetic frustules (Fig. 4B, black) after incubation with TLS11a (Fig. 4B, red) is further evidence of successful surface functionalization. Photoluminescence emission spectra (Fig. 4C) show a broad and strong emission profile between 450 nm and 750 nm when excited at 450 nm.[50–52]

Prior to performing on-chip magnetophoresis, we optimized the position of the magnets and the geometry of the microfluidic channel in the magnetic separation zone, using computational fluid dynamics (CFD) simulations. Pseudo-transient simulations were run in Ansys Fluent v.2020 (Ansys Inc., Canonsburg, USA), by coupling the magneto-hydrodynamic module (MHD) with the solution of the Navier-Stokes equations. Details on the computational domain, the simulated fluid (mixture of human blood and 0.1% PEO), boundary conditions for the fluid and magnetic component and numerical settings are reported in the Supplementary Information. Simulations indicated that that the location of the

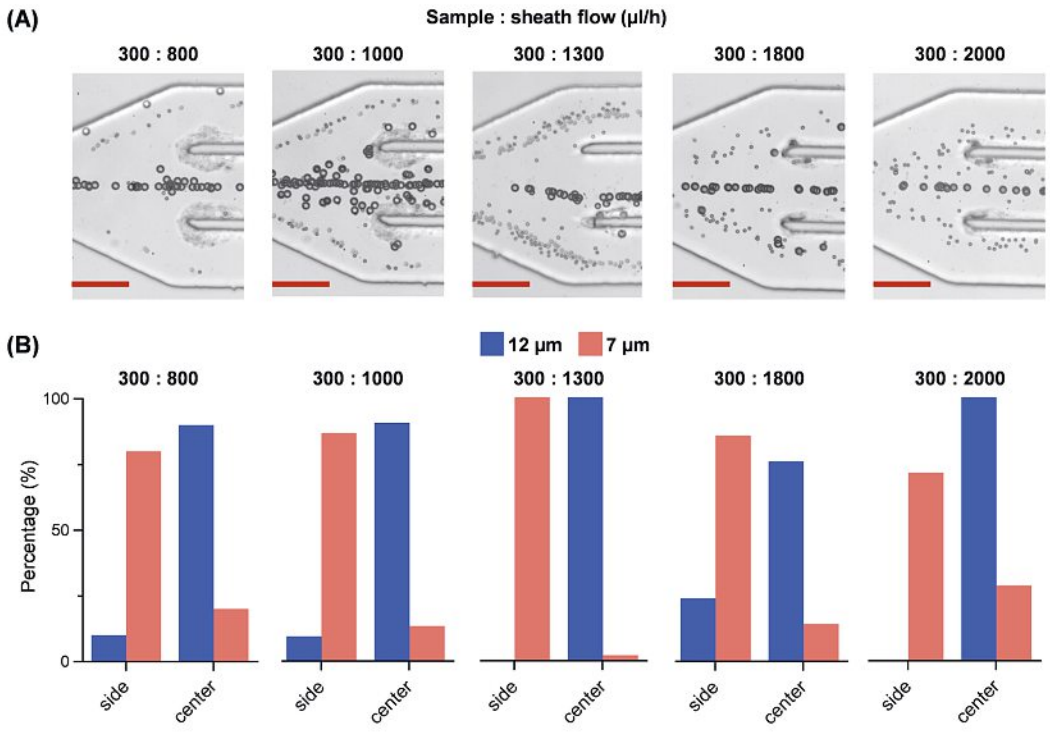

Fig. 2. Performance of the hybrid microfluidic device. Microfluidic separation at various combination of flow rates was performed using 7 and 12 µm diameter PS beads at different sample:sheath flow rates. The sample flow contains 0.1% PEO and the sheath flow contains 0.3% PEO. (A) Images of the 7 and 12 µm PS bead separation process at different sample:sheath flow rates. (B) Separation efficiencies of the 7 and 12 µm particles at different sample:sheath flow rates. The best performance was observed at a sample: sheath flow rate 300:1300 µl/h. Scale bars: 50 µm.

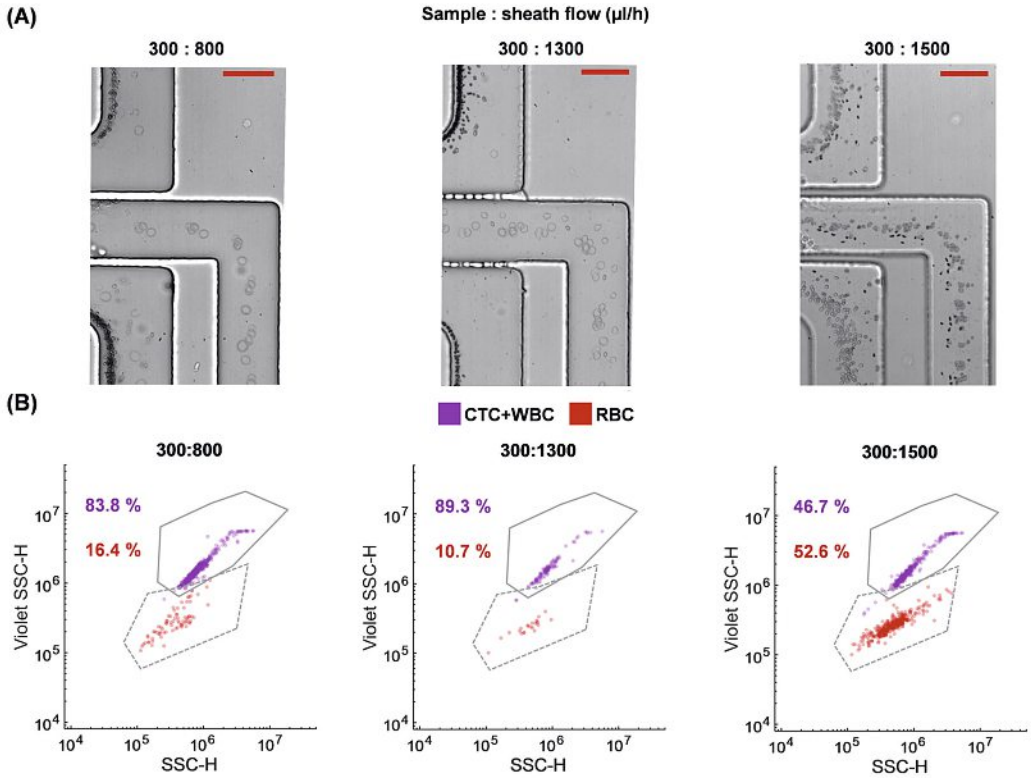

Fig. 3. Passive separation of HepG2 CTCs and WBCs from RBCs. The separation was performed using whole blood and three different combinations of sample:sheath flow rates. The sheath flow contains 0.3% PEO. (A) Images of the viscoelastic separation in various flow rate combinations. (B) Side scatter plots obtained from the central outlet. The RBC population (red) and the WBC+CTC population (purple) were distinguished using 405 nm side scatter (SSC-H) and 488nm side scatter (violet SSC-H) signals. The best separation was observed in 300: 1300 ml/h sample:sheath flow rate. Scale bars: 50 µm in length.

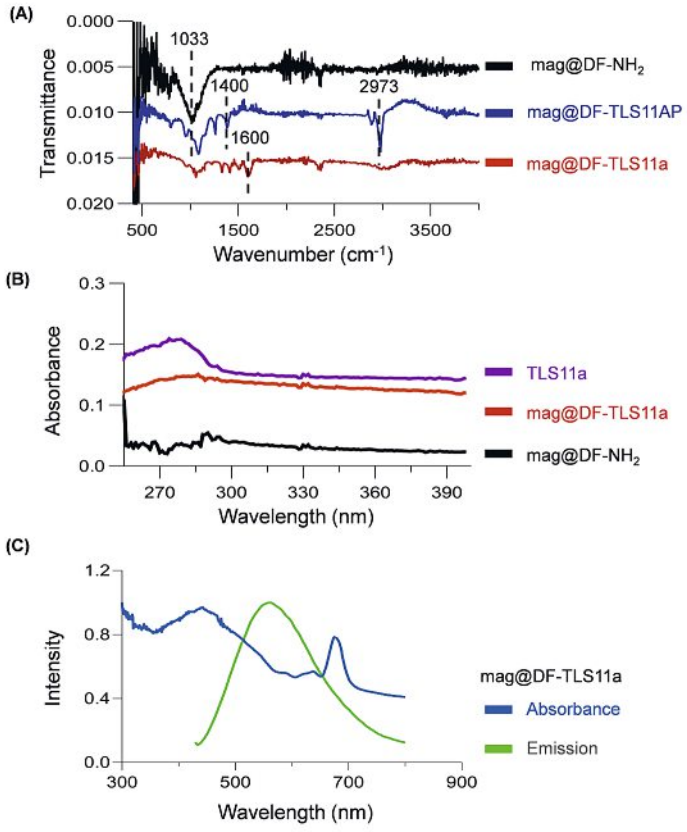

Fig. 4. Spectroscopic characterization of the diatomic frustules (DF), and their subsequent functionalization with magnetic diatomic frustules (mag@DF) and the TLS11a aptamer (mag@DF–TLS11a). (A) FTIR spectra of the mag@DF before (black) and after functionalization with APTES (blue) and TLS11a (red). (B) Absorption spectra of the mag@DF–TLS11a frustules, pure TLS11a and mag@DF. (C) Absorbance (blue) and emission (green) spectra of the mag@DF-TLS11a complexes. The excitation wavelength for the emission spectra was at 450nm.

neodymium magnets has a significant effect on CTC separation efficiency. Whilst the velocity field is only negligibly modified by the magnetic field, the path of injected paramagnetic particles (mimicking CTCs) was highly influenced by the magnetic field which exerts a force on magnetized cells in the sorting area (Fig. S5). The computational simulations also revealed that in the absence of the magnetic field, CTCs would not be separated from other cells, but would rather be driven into channel outlet 2.

Based on the results of these simulations, the magnetophoresis zone was designed in two parts. The first being a long, narrow rectangular microchannel (50 µm wide, 50 µm high and 14 mm long) to focus the WBCs and CTCs into a single file. Such an extended microchannel provides adequate time for cells to move and focus at the channel centerline, thus ensuring that they all experience a constant magnetic field. Focusing also ensures that cells are evenly distributed within the channel, preventing localized concentrations that would perturb the magnetic field and disrupt separation. The second part of the magnetophoresis zone contains a much wider channel (50 µm high, 800 wide µm and 2 cm long) feeding two outlets. To facilitate magnetic sorting, we placed neodymium magnets at the optimized locations along a single wall of the chip (Fig. S5). The additional width of the channel leads to a significant decrease in the velocity of the passing cells (from 0.17 m/s to 0.0112 m/s), increasing the residence time in the magnetic field and decreasing the effect of inertial forces. This improves the magnetic separation efficiency by ensuring that cells have adequate time to migrate towards the external magnetic field. To facilitate separation of non-magnetized cells (*e.g.* WBCs) we designed two outlets with specific geometries. The downstream outlet (outlet 3) was long and narrow, so as to increase hydraulic pressure. Thus, in the absence of a magnetic force, cells flow towards the upstream outlet (outlet 2) as this is the path of least resistance. By applying a magnetic force along the wall of the high-resistance outlet (outlet 3), it was expected that magnetized cells (*i.e.* CTCs tagged with magnetic frustules) would separate from the bulk population. To confirm this behaviour,

we introduced HepG2 CTCs tagged with TLS11a-functionalized magnetic frustules (Figs S6 and S7) into the microfluidic device, with and without the neodymium magnets installed. As expected, in the presence of the magnet field the majority of the cells are deviated and driven through outlet 3. Conversely, in the absence of the magnets all cells exit from outlet 2. These data confirm that the designed system is able to efficiently separate magnetically tagged HepG2 CTCs.

Passive–Active Purification of CTCs from Blood Samples

After successful optimization of both the passive and active separation functionalities, we then assessed the capacity of the microfluidic device to separate CTCs from WBCs and RBCs in whole blood. We spiked whole blood with HepG2 CTCs tagged with TLS11a-functionalised magnetic frustules and flowed them through the device under the previously optimized parameters. The eluent from each outlet was collected, analyzed using flow cytometry, and compared to the unprocessed input sample (Fig. 5). Platelets were gated from RBCs, WBCs, and CTCs as described in the Experimental Section, and identification of CTCs within this subpopulation was achieved by exploiting the innate fluorescence of the magnetic frustules in the green (520 nm, FITC) and red (660 nm, APC) channels (Fig. 5). The scatter-plots indicate that the cell mixture was distinctly separated into two populations of CTCs and WBCs. In this regard, it should be noted that use of frustules as multi-color labels is especially advantageous, and greatly improves the separation of CTCs and WBCs when compared a one-color detection approach (Fig. S8). In addition, and contrary to most separation methodologies, magnetic and fluorescent labeling of CTCs is performed in a single step and does not require the use of fluorescently labeled antibodies or aptamers. Analysis of the eluents clearly demonstrates the ability of our platform to separate CTCs from WBCs and RBCs. Specifically, the eluent from outlet 1 consists mainly of RBCs (95%), followed by WBCs (4.2%) and trace amounts of CTCs (0.8%). The eluent from outlet 2 consists of 49% WBCs, 45% RBCs and 6% CTCs. Finally, the eluent from outlet 3 is significantly enriched with CTCs (89.1%), with smaller amounts of RBCs (7.6%) and WBCs (3.3%). These data were consistent with our expectations, and can be simply rationalized. Enrichment of the RBCs in outlet 1 confirms viscoelastic focusing of larger WBCs and CTCs towards the central channel, and smaller RBCs towards the side-channel outlet. Similarly, enrichment of the WBCs in outlet 2 and CTCs from outlet 3 confirms that magnetic separation of these two nucleated populations occurs on-chip. WBCs are not magnetized by the frustules and thus flow along the path of least resistance (towards outlet 2), whereas the magnetized CTCs are directed towards outlet 3. The recovery rate and purity values of the CTCs were 94.6% and 89.7%, respectively. Immunomagnetic isolation and magnetophoresis based on labelling target cells with magnetic particles have been widely used for the isolation of CTCs. For example, Huang *et al.* reported a two-step isolation method including a first pre-enrichment step *via* Dean flow fractionation to remove RBCs and a second magnetophoretic step for the separation of CTCs from WBCs.[33] Such an approach yielded a separation efficiency of 83% and a purity of 19% for separation of CTCs from diluted blood ($1/10^5$ ratio CTCs to blood cells). Interestingly, our approach can achieve significantly better purity at a higher ratio of CTCs to blood cells ($1/10^7$), albeit in a lower flow rate regime. Nasiri *et al.* presented a hybrid microfluidic device composed of inertial and magnetophoresis-based separators, and achieved a separation efficiency of 95% and a purity of 93% (for a 1:1000 ratio of CTCs to blood cells). Our approach yields similar values for both separation efficiency and purity, but at significantly higher ($1/10^7$) ratios of CTCs to blood cells.[34] Despite the fact that the viscoelastic separation approach is effective at lower flow rates than inertial regimes, our hybrid sorting technique can reliably achieve some of the highest recovery rates (~95%) and purities (~90%) for hybrid devices in the literature. These numbers are especially encouraging, particularly when considering the complexity of the initial sample matrix and the necessity of a multi-step purification process, and demonstrate the power of this dual passive–active approach for separating CTCs from complex matrices.

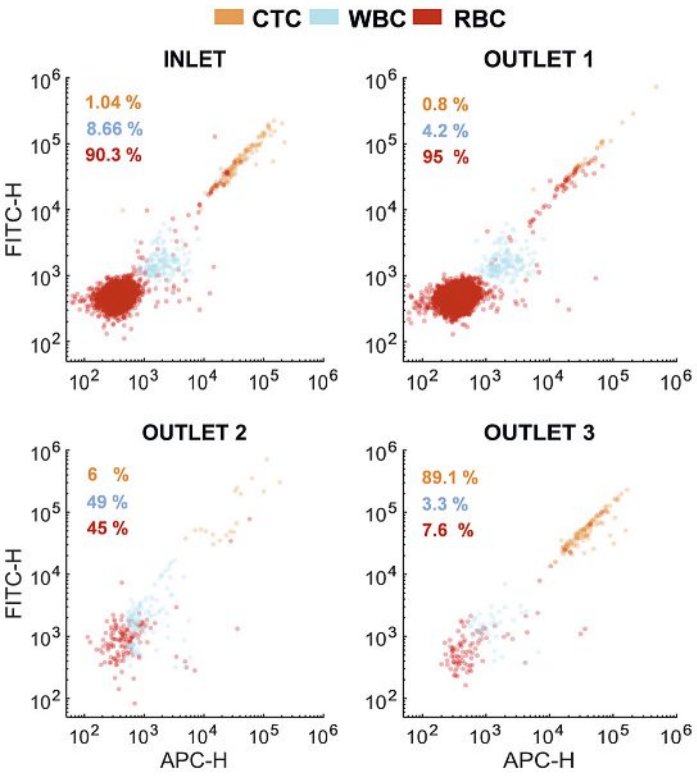

Fig. 5. Particle separation results derived from dual color APC-H (fluorescence height at 660nm) against FITC-A (fluorescence height at 520 nm) scatter log–log plots. Flow cytometry dual color graphs show the percentages of RBCs, WBCs and functionalized HepG2 CTCs from the inlet and each outlet of the hybrid microfluidic device.

Conclusions

To conclude, we have developed a microfluidic platform for separating disease-specific CTCs from complex blood samples, without the need for any sample pre-treatment. The described microfluidic method combines passive viscoelastic size-based separation with active magnetophoresis to effectively separate CTCs from WBCs and RBCs present in whole blood. We studied the effects of varying both sheath and sample flow rates, as well as the addition of PEO, and determined that viscoelastic separation efficiency is a function of both the elastic and inertial forces exerted upon the sample. Magnetization of the CTCs was achieved by tagging with aptamer-functionalized magnetic diatomic biosilica frustules, a hitherto unexplored method for isolating CTCs in microfluidic systems. In addition, biosilica frustules can also serve as multi-color fluorescent labels, resulting in absolute quantification of CTCs in blood by flow cytometry. The use of biosilica frustules has potential to significantly impact flow cytometry studies. With their broad absorption spectra, they can be excited using a variety of wavelengths. Small molecule fluorophores conventionally used in flow cytometry have narrow absorption spectra and thus cannot be used as multi-wavelength emission fluorophores. By combining strategic integration of neodymium magnets and bespoke microfluidic geometries, we

achieved successful magnetophoretic separation of frustule-tagged CTCs. Finally, the performance of the entire integrated chip was assessed by separating HepG2-derived CTCs from WBCs and RBCs in unprocessed whole blood, with a recovery rate of 94.6% and purity of 89.7% being achieved. Given the ubiquity of cell separation and cytology within modern medicine and basic research, we believe that the platform holds significant diagnostic value. Moreover, the simplicity of the device compared to existing technologies offers a lower point of entry for non-experts. We anticipate that this simplicity of this approach will lead to increased adoption of the technology for multiple related applications.

Supporting Information

Experimental details and supplemental figures/tables are available as a PDF on https://chimia.ch/chimia. Movie S1: High-speed video of viscoelastic separation of HepG2+WBCs cells from RBCs in blood.

Author Contributions

R.M. & M.A. carried out the experimental work. A.dM., D.A.R. and S.S. wrote the manuscript. R.M. & M.C. planned and carried out the CFD simulations. Z.V., S.S., A.dM. and H.N. supervised the project. All authors discussed the results and contributed to the final manuscript.

Acknowledgements

R.M. acknowledges funding from Tarbiat Modarres University (Tehran, Iran), D.A.R. acknowledges funding from the European Union's Horizon 2020 research and innovation programme under the Marie Skłodowska-Curie grant agreement 840232. M.C. acknowledges funding from Foundation Botnar (Basel, Switzerland).

Received: July 4, 2022

[1] C. Wang, M. Ye, L. Cheng, R. Li, W. Zhu, Z. Shi, C. Fan, J. He, J. Liu, Z. Liu, *Biomaterials* **2015**, *54*, 55, https://doi.org/10.1016/j.biomaterials.2015.03.004.
[2] M. V Nesterova, N. Johnson, C. Cheadle, S. E. Bates, S. Mani, C. A. Stratakis, I. Kahn, R. K. Gupta, Y. S. Cho-Chung, *Cancer Res.* **2006**, *66*, 8971, https://doi.org/10.1158/0008-5472.CAN-06-1049.
[3] P. Bankó, S. Y. Lee, V. Nagygyörgy, M. Zrínyi, C. H. Chae, D. H. Cho, A. Telekes, *J. Hematol. Oncol.* **2019**, *12*, 48, https://doi.org/10.1186/s13045-019-0735-4.
[4] W. Sheng, T. Chen, R. Kamath, X. Xiong, W. Tan, Z. H. Fan, *Anal. Chem.* **2012**, *84*, 4199, https://doi.org/10.1021/ac3005633.
[5] L. Descamps, D. Le Roy, A. L. Deman, *Int. J. Mol. Sci.* **2022**, *23*, https://doi.org/10.3390/ijms23041981.
[6] W. Liang, J. Liu, X. Yang, Q. Zhang, W. Yang, H. Zhang, L. Liu, *Microfluid. Nanofluid.* **2020**, *24*, https://doi.org/10.1007/s10404-020-2331-x.
[7] S. H. Au, J. Edd, A. E. Stoddard, K. H. K. Wong, F. Fachin, S. Maheswaran, D. A. Haber, S. L. Stott, R. Kapur, M. Toner, *Sci. Rep.* **2017**, *7*, 1, https://doi.org/10.1038/s41598-017-01150-3.
[8] Z. Liu, Y. Huang, W. Liang, J. Bai, H. Feng, Z. Fang, G. Tian, Y. Zhu, H. Zhang, Y. Wang, A. Liu, Y. Chen, *Lab on a Chip* **2021**, *21*, 2881, https://doi.org/10.1039/D1LC00360G.
[9] H. Xu, Z. P. Aguilar, L. Yang, M. Kuang, H. Duan, Y. Xiong, H. Wei, A. Wang, *Biomaterials* **2011**, *32*, 9758, https://doi.org/10.1016/j.biomaterials.2011.08.076.
[10] C. M. Earhart, C. E. Hughes, R. S. Gaster, C. C. Ooi, R. J. Wilson, L. Y. Zhou, E. W. Humke, L. Xu, D. J. Wong, S. B. Willingham, E. J. Schwartz, I. L. Weissman, S. S. Jeffrey, J. W. Neal, R. Rohatgi, H. A. Wakelee, S. X. Wang, *Lab Chip* **2014**, *14*, 78, https://doi.org/10.1039/c3lc50580d.
[11] P. Y. Chu, C. J. Liao, C. H. Hsieh, H. M. Wang, W. P. Chou, P. H. Chen, M. H. Wu, *Sensors and Actuators, B: Chem.* **2019**, *283*, 621, https://doi.org/10.1016/j.snb.2018.12.047.
[12] C. J. Liao, C. H. Hsieh, T. K. Chiu, Y. X. Zhu, H. M. Wang, F. C. Hung, W. P. Chou, M. H. Wu, *Micromachines (Basel)* **2018**, *9*, https://doi.org/10.3390/mi9110563.
[13] K. Wang, W. Zhou, Z. Lin, F. Cai, F. Li, J. Wu, L. Meng, L. Niu, H. Zheng, *Sensors and Actuators, B: Chem.* **2018**, *258*, 1174, https://doi.org/10.1016/j.snb.2017.12.013.
[14] M. Wu, P. H. Huang, R. Zhang, Z. Mao, C. Chen, G. Kemeny, P. Li, A. V. Lee, R. Gyanchandani, A. J. Armstrong, M. Dao, S. Suresh, T. J. Huang, *Small* **2020**, *16*, 2004438, https://doi.org/10.1002/smll.202004438.
[15] P. Augustsson, C. Magnusson, M. Nordin, H. Lilja, T. Laurell, *Anal. Chem.* **2012**, *84*, 7954, https://doi.org/10.1021/ac301723s.
[16] J. M. Martel, M. Toner, *Annu. Rev. Biomed. Eng.* **2014**, *16*, 371, https://doi.org/10.1146/annurev-bioeng-121813-120704.
[17] T. Luo, L. Fan, Y. Zeng, Y. Liu, S. Chen, Q. Tan, R. H. W. Lam, D. Sun, *Lab Chip* **2018**, *18*, 1521, https://doi.org/10.1039/C8LC00173A.
[18] J. Zhang, D. Yuan, Q. Zhao, S. Yan, S. Y. Tang, S. H. Tan, J. Guo, H. Xia, N. T. Nguyen, W. Li, *Sensors and Actuators, B: Chem.* **2018**, *267*, 14, https://doi.org/10.1016/j.snb.2018.04.020.
[19] H. Luo, C. Zhao, K. Song, D. Liu, W. Ma, X. Yu, H. Su, Z. Zhang, Y. Zohar, Y. K. Lee, *Microfluid. Nanofluid.* **2019**, *23*, 1, https://doi.org/10.1007/s10404-019-2240-z.
[20] Y. Zhou, Z. Ma, Y. Ai, *RSC Adv.* **2019**, *9*, 31186, https://doi.org/10.1039/c9ra01792e.
[21] E. Ozkumur, A. M. Shah, J. C. Ciciliano, B. L. Emmink, D. T. Miyamoto, E. Brachtel, M. Yu, P. I. Chen, B. Morgan, J. Trautwein, A. Kimura, S. Sengupta, S. L. Stott, N. M. Karabacak, T. A. Barber, J. R. Walsh, K. Smith, P. S. Spuhler, J. P. Sullivan, R. J. Lee, D. T. Ting, X. Luo, A. T. Shaw, A. Bardia, L. V. Sequist, D. N. Louis, S. Maheswaran, R. Kapur, D. A. Haber, M. Toner, *Sci. Transl. Med.* **2013**, *5*, 1, https://doi.org/10.1126/scitranslmed.3005616.
[22] M. Asghari, X. Cao, B. Mateescu, D. van Leeuwen, M. K. Aslan, S. Stavrakis, A. J. deMello, *ACS Nano* **2020**, *14*, 422, https://doi.org/10.1021/acsnano.9b06123.
[23] X. Lu, C. Liu, G. Hu, X. Xuan, *J. Coll. Interf. Sci.* **2017**, *500*, 182, https://doi.org/10.1016/j.jcis.2017.04.019.
[24] J. Zhou, I. Papautsky, *Microsyst. Nanoeng.* **2020**, *6*, 113, https://doi.org/10.1038/s41378-020-00218-x.
[25] F. Tian, W. Zhang, L. Cai, S. Li, G. Hu, Y. Cong, C. Liu, T. Li, J. Sun, *Lab Chip* **2017**, *17*, 3078, https://doi.org/10.1039/c7lc00671c.
[26] F. Tian, L. Cai, J. Chang, S. Li, C. Liu, T. Li, J. Sun, *Lab Chip* **2018**, *18*, 3436, https://doi.org/10.1039/c8lc00700d.
[27] C. Liu, C. Xue, X. Chen, L. Shan, Y. Tian, G. Hu, *Anal. Chem.* **2015**, *87*, 6041, https://doi.org/10.1021/acs.analchem.5b00516.
[28] A. Myklatun, M. Cappetta, M. Winklhofer, V. Ntziachristos, G. G. Westmeyer, *Sci. Rep.* **2017**, *7*, 6942, https://doi.org/10.1038/s41598-017-06946-x.
[29] K. Hoshino, Y. Y. Huang, N. Lane, M. Huebschman, J. W. Uhr, E. P. Frenkel, X. Zhang, *Lab Chip* **2011**, *11*, 3449, https://doi.org/10.1039/c1lc20270g.
[30] F. Alnaimat, S. Dagher, B. Mathew, A. Hilal-Alnqbi, S. Khashan, *Chem. Rec.* **2018**, *18*, 1596, https://doi.org/10.1002/tcr.201800018.
[31] L. Luo, Y. He, *Cancer Med.* **2020**, *9*, 4207, https://doi.org/10.1002/cam4.3077.
[32] A. N. Surendran, R. Zhou, Y. Lin, *J. Med. Devices* **2021**, *15*, 1, https://doi.org/10.1115/1.4048912.
[33] D. Huang, N. Xiang, *Lab Chip* **2021**, *21*, 1409, https://doi.org/10.1039/D0LC01223H.
[34] R. Nasiri, A. Shamloo, J. Akbari, *Micromachines (Basel)* **2021**, *12*, https://doi.org/10.3390/mi12080877.
[35] A. K. Gupta, M. Gupta, *Biomaterials* **2005**, *26*, 1565, https://doi.org/10.1016/j.biomaterials.2004.05.022.
[36] J. Esfandyari, B. Shojaedin-Givi, H. Hashemzadeh, M. Mozafari-Nia, Z. Vaezi, H. Naderi-Manesh, *Photodiag. Photodyn. Ther.* **2020**, *30*, 101753, https://doi.org/10.1016/j.pdpdt.2020.101753.
[37] M. de Stefano, L. de Stefano, *J. Nanosci. Nanotechnol.* **2005**, *5*, 15, https://doi.org/10.1166/jnn.2005.001.
[38] I. Rea, M. Terracciano, L. de Stefano, *Adv. Healthc. Mater.* **2017**, *6*, 1601125, https://doi.org/10.1002/adhm.201601125.
[39] L. de Stefano, A. Lamberti, L. Rotiroti, M. de Stefano, *Acta Biomater.* **2008**, *4*, 126, https://doi.org/10.1016/j.actbio.2007.09.003.
[40] J. Delasoie, F. Zobi, *Pharmaceutics* **2019**, *11*, 537, https://doi.org/10.3390/pharmaceutics11100537.
[41] S. Leonardo, B. Prieto-Simón, M. Campàs, *TrAC* **2016**, *79*, 276, https://doi.org/10.1016/j.trac.2015.11.022.
[42] P. Gholami, A. Khataee, A. Bhatnagar, B. Vahid, *ACS Appl. Mater. Interf.* **2021**, *13*, 13072, https://doi.org/10.1021/acsami.0c21076.
[43] G. Holzner, S. Stavrakis, A. deMello, *Anal. Chem.* **2017**, *89*, 11653, https://doi.org/10.1021/acs.analchem.7b03093.
[44] A. Mehran, P. Rostami, M. S. Saidi, B. Firoozabadi, N. Kashaninejad, *Biosensors (Basel)* **2021**, *11*, https://doi.org/10.3390/bios11110406.
[45] P. Liu, H. Liu, D. Yuan, D. Jang, S. Yan, M. Li, *Anal. Chem.* **2021**, *93*, 1586, https://doi.org/10.1021/acs.analchem.0c03990.
[46] S. W. Ahn, S. S. Lee, S. J. Lee, J. M. Kim, *Chem. Eng. Sci.* **2015**, *126*, 237, https://doi.org/10.1016/j.ces.2014.12.019.
[47] D. Sun, J. Lu, X. Wang, Y. Zhang, Z. Chen, *Microchim. Acta* **2017**, *184*, 3487, https://doi.org/10.1007/s00604-017-2376-z.
[48] R. Gao, C. Zhan, C. Wu, Y. Lu, B. Cao, J. Huang, F. Wang, L. Yu, *Lab Chip* **2021**, *21*, 3888, https://doi.org/10.1039/D1LC00516B.
[49] Y. Zheng, C. Zhang, Z. Lai, Y. Zeng, J. Li, D. Zhang, X. Liu, *Nanoscale* **2021**, *13*, 11279, https://doi.org/10.1039/D1NR00836F.

[50] T. Qin, T. Gutu, J. Jiao, C. H. Chang, G. L. Rorrer, *J. Nanosci. Nanotechnol*. **2008**, *8*, 2392, https://doi.org/10.1166/jnn.2008.241.
[51] N. Mazumder, A. Gogoi, R. D. Kalita, G. A. Ahmed, A. K. Buragohain, A. Choudhury, *Ind. J. .Phys.* **2010**, *84*, 665, https://doi.org/10.1007/s12648-010-0068-1.
[52] M. Sprynskyy, P. Pomastowski, M. Hornowska, A. Król, K. Rafińska, B. Buszewski, *Mater. Design* **2017**, *132*, 22, https://doi.org/10.1016/j.matdes.2017.06.044.

License and Terms

The definitive version of this article is the electronic one that can be found at https://doi.org/10.2533/chimia.2022.661